



**Michigan  
Technological  
University**

Michigan Technological University  
**Digital Commons @ Michigan Tech**

---

Michigan Tech Publications

---

3-29-2023

## Effect of the Dynamic Froude–Krylov Force on Energy Extraction from a Point Absorber Wave Energy Converter with an Hourglass-Shaped Buoy

Houssein Yassin

*Michigan Technological University, hyassin@mtu.edu*

Tania Demonte Gonzalez

*Michigan Technological University*

Gordon Parker

*Michigan Technological University, ggparker@mtu.edu*

David Wilson

*Sandia National Laboratories, New Mexico*

Follow this and additional works at: <https://digitalcommons.mtu.edu/michigantech-p>



Part of the [Mechanical Engineering Commons](#)

---

### Recommended Citation

Yassin, H., Demonte Gonzalez, T., Parker, G., & Wilson, D. (2023). Effect of the Dynamic Froude–Krylov Force on Energy Extraction from a Point Absorber Wave Energy Converter with an Hourglass-Shaped Buoy. *Applied Sciences (Switzerland)*, 13(7). <http://doi.org/10.3390/app13074316>  
Retrieved from: <https://digitalcommons.mtu.edu/michigantech-p/17073>





Follow this and additional works at: <https://digitalcommons.mtu.edu/michigantech-p>



Part of the [Mechanical Engineering Commons](#)

## Article

# Effect of the Dynamic Froude–Krylov Force on Energy Extraction from a Point Absorber Wave Energy Converter with an Hourglass-Shaped Buoy

Houssein Yassin <sup>1,†</sup> , Tania Demonte Gonzalez <sup>1,†</sup> , Gordon Parker <sup>1,\*,†</sup>  and David Wilson <sup>2,†</sup> 

<sup>1</sup> Mechanical Engineering–Engineering Mechanics Department, Michigan Technological University, Houghton, MI 49931, USA

<sup>2</sup> Sandia National Laboratories, Albuquerque, NM 87185, USA

\* Correspondence: ggparker@mtu.edu; Tel.: +1-(906)-370-1341

† These authors contributed equally to this work.

**Abstract:** Point absorber wave energy converter (WEC) control strategies often require accurate models for maximum energy extraction. While linear models are suitable for small motions, the focus is on the nonlinear model of an hour-glass shaped buoy undergoing large vertical displacements. Closed-form expressions for the static and dynamic Froude–Krylov forces are developed. It is shown that, in general, the dynamic and static forces are of similar magnitude, which is not the case for a spherical buoy. While the dynamic force reduces the amplitude of the net buoy force, its shape predicts a larger buoy response than if neglected, causing the nonlinear terms to have an even more significant effect. An input-state feedback linearizing controller is developed to show how the nonlinear model can be used in a control law. A 2.5 m buoy example is simulated to illustrate the approach of tracking an arbitrary displacement reference. For the case considered, the extracted power is 30% larger when the nonlinear dynamic FK force is used in the control law. The hourglass buoy is also compared to a spherical buoy to illustrate differences in their response to regular waves and energy extraction when using the same control laws. A spherical buoy diameter of 7.5 m was required to obtain the same power output as a 5 m tall hourglass buoy. A power-force-amplitude (PFA) metric is introduced to compare energy extraction performance and power take-off requirements. The hourglass buoy's PFA was 13% larger than the spherical buoy implying that it can produce similar power but with less control effort.

**Keywords:** wave energy; nonlinear model; Froude–Krylov force; input-state feedback linearization; power-force-amplitude



**Citation:** Yassin, H.; Demonte Gonzalez, T.; Parker, G.; Wilson, D. Effect of the Dynamic Froude–Krylov Force on Energy Extraction from a Point Absorber Wave Energy Converter with an Hourglass-Shaped Buoy. *Appl. Sci.* **2023**, *13*, 4316. <https://doi.org/10.3390/app13074316>

Academic Editors: Átila Madureira Bueno, Diego Colón, José Balthazar and Angelo Marcelo Tusset

Received: 17 February 2023

Revised: 22 March 2023

Accepted: 27 March 2023

Published: 29 March 2023



**Copyright:** © 2023 by the authors. Licensee MDPI, Basel, Switzerland. This article is an open access article distributed under the terms and conditions of the Creative Commons Attribution (CC BY) license (<https://creativecommons.org/licenses/by/4.0/>).

## 1. Introduction

Sea waves are an attractive source of energy due to their relatively large energy density as compared to solar and wind resources [1]. This same high-energy sea environment conspires against the widespread use of wave energy converters (WECs) due to engineering challenges, including extreme event survivability and maintenance [2–5]. Extracting energy and transferring it to a load efficiently is a WEC's typical objective. Harmonizing its mechanical, power take-off (PTO), and control strategy designs may lead to the practical application of WECs for terrestrial and at-sea energy grids.

A point absorber WEC's PTO extracts energy from the relative velocity between its floating buoy and fixed base. By definition, maximum energy extraction is achieved by controlling its PTO force such that the integrated product of the force and relative velocity is maximized subject to the PTO's force and stroke limits. At times the PTO will do work on the buoy, momentarily sacrificing energy extraction to produce a buoy response leading to greater energy extraction later. Energy optimal control has been studied extensively for assumed buoy geometries, including quantifying upper bounds [1,6,7], impedance

matching [7–11], and both closed-form [12] and numerical optimal control solutions [13] such as with model predictive control [14–16]. Early efforts focused on buoy response regimes that can be modeled using linear differential equations considering a buoy's nonlinear response a more recent focus [17–19].

While this paper investigates a particular buoy geometry, the hourglass shape of Wilson et al. [17,20,21], it is important to note that understanding mechanical energy extraction is only part of the more complex problem of energy production. Addressing this system-level objective requires simultaneous consideration of the entire process, including the design of the WEC, its PTO, and electrical energy transmission power electronics [22].

Since a point absorber's buoy shape and mass affects its dynamics response, the shape is a crucial design consideration and should be exploited. Garcia et al. [23,24] quantified the benefit of the simultaneous design of a point absorber's buoy geometry and control law. Adaptive shape modification is another method for expanding the performance of a WEC operating in off-nominal sea conditions [25]. The review article by Garcia and Forehand provides a comprehensive accounting of past and current efforts in shape optimization, clearly illustrating the importance of geometry for a broad range of WEC types.

While buoy shape affects a WEC's model form when operating in a linear regime, it can profoundly affect its nonlinear model and response. Computational fluid dynamics (CFD) models can capture these effects but are impractical for real-time, model-based control laws [26]. Closed-form nonlinear Froude–Krylov (FK) force models have been developed in [27–29] to incorporate buoy shape effects into model-based control laws for large-motion, nonlinear operating regimes. Giorgi et al. [27] present an analytical approach with 2% error to derive the nonlinear FK forces using Airy's wave theory for deep water waves to represent the static and dynamic pressure forces acting on the buoy.

Researchers have proposed various control strategies that incorporate the analytical nonlinear FK forces. The authors in [30,31] developed a sliding mode controller for a heaving point absorber that demonstrated the robustness and energy maximization of the WEC. In [32], an optimal model-based control was developed for a data-based modeled heaving point absorber. The latching control is a well-established technique that has also been used in WECs, including those that utilize the computationally efficient closed-form nonlinear FK forces [26,33,34]. All of these papers have used conventional buoy shapes such as spheres and cylinders, which have well-studied hydrodynamics. In this study, a state feedback linearization control scheme is proposed for an unconventional hourglass-shaped heaving point absorber.

An hourglass-shaped, point absorber buoy was considered in three recent articles by Wilson et al. [17,20,21] and is the motivation for this paper. In [20], the authors developed the hourglass-shaped buoy's nonlinear hydrostatic force term and compared its energy extraction performance to a cylindrical buoy. Using the results from [35], where a cubic term was inserted into the cylindrical buoy's control strategy, the authors recreated the effect naturally through the hourglass shape of the buoy. They showed that the hourglass buoy provided the same reactive power management as the nonlinear control of [35] using a velocity feedback control law. In [17], the hourglass buoy control was extended further using the Hamiltonian surface shaping and power flow control (HSSPFC) technique. The model for the hourglass buoy was the same as [20] where again, the dynamic Froude–Krylov force was not included. The energy extraction performance of the hourglass buoy was compared to a cylindrical buoy with an artificially applied cubic nonlinearity. A key result was that the hourglass buoy, containing the natural cubic nonlinearity, outperformed the cylindrical buoy with the artificial cubic term. In [21], a rate feedback control strategy was used for an hourglass-shaped buoy point absorber capable of adapting its cone angle based on incident wave conditions. Using an irregular wave example, it was shown that the energy extraction increased by 50% when the cone angle was varied. The model used for the simulation was the same as described previously.

The goal of this paper is to explore the effect of the nonlinear dynamic Froude–Krylov force, derived using the approach of Giorgi and Ringwood [27], on an hourglass-shaped

buoy point absorber. We first examine the buoy's simulated response to regular waves with and without the dynamic FK force in the model. It is shown that neglecting this term can lead to underprediction of the buoy motion in some cases. Thus, it should be included in the analysis and model-based control system design. Adjusting the draft could potentially increase the energy extracted, as shown on a spherical buoy in [36]. However, for the hourglass-shaped buoy, varying the draft leads to additional terms in the static and dynamic Froude–Krylov force expressions. Therefore, in this study, the considered buoy's draft is at its vertical midpoint in all cases. A feedback linearizing controller is used to investigate further the effect of including the dynamic FK force term in the hourglass-shaped buoy's PTO control law. It should be noted that this control strategy is provided merely as an example of how the nonlinear model can be used in a model-based control strategy. A sinusoidal reference trajectory is used but is not presumed to be optimal from an energy extraction perspective. Finally, the closed-loop energy extraction performance of hourglass and spherical buoys are compared using the previously mentioned feedback linearizing controller, where the nonlinear models are used for each of their control laws. This is performed to illustrate the unique behavior of the hourglass shape to help explain why it extracts greater energy than a similarly sized spherical buoy.

This article has three contributions. First, the closed-form dynamic Froude–Krylov force expression for an hourglass-shaped buoy was developed. Second, we show that the dynamic Froude–Krylov force of an hourglass-shaped buoy is not negligible and should be considered during analysis and control system design. Third, the closed-loop energy extraction of an hourglass point absorber is greater than a similarly sized spherical device.

The remainder of this paper is organized as follows. Section 2 describes the model used by the simulation and the control law, including developing the hourglass buoy's FK forces. Section 3 shows the contributions of the static and dynamic FK forces to the buoy's free response. Section 4 develops the feedback linearization control law used for evaluating the performance of the hourglass and spherical buoys whose FK force model is described in Section 5. The results of a simulated case study are provided in Section 6 with concluding remarks in Section 7.

## 2. Hourglass Buoy Model

The buoy of mass  $m$  and weight  $F_g$  has the geometry shown in Figure 1 where its dynamic model of Equation (1) is used for simulation, assessing energy extraction performance, and by the model-based control law.

$$m\ddot{\zeta} = F_g + F_{fk,s} + F_{fk,d} + F_r + F_c \quad (1)$$

The buoy is constrained to heave with potentially large vertical displacement  $\zeta$  defined relative to the still water line. This assumption simplifies the model considerably compared to general motion, and state space models such as used in [37]. The nonlinear static and dynamic Froude–Krylov forces,  $F_{fk,s}$  and  $F_{fk,d}$ , are the main focus of this work and are developed in Section 2.1. The radiation force model,  $F_r$ , is described in Section 2.2, and the power take-off (PTO) device is assumed to be ideal and applies  $F_c$  to the buoy according to the control law of Section 4.

It is assumed that the waves are regular with their elevation given by Equation (2). The waves are also assumed to be linear with steepness,  $S_w = 2A/\lambda \leq 0.018$ , and wavelength,  $\lambda$ , much greater than the buoy's maximum diameter or  $\lambda \gg 2h \tan(\alpha)$  and are the justification for neglecting the diffraction forces [8].

$$\eta = A \cos(\omega t) \quad (2)$$

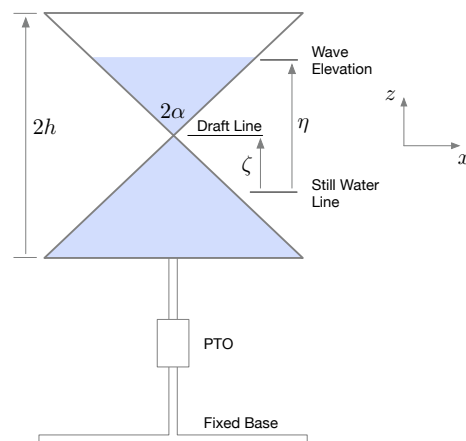


**Figure 1.** Hourglass buoy, notation, and coordinate system. Blue denotes the submerged volume.

### 2.1. Froude–Krylov Force

The Froude–Krylov (FK) force,  $F_{fk}$  of Equation (3), is the integration of the pressure field forces,  $\vec{P}(t)$ , over the instantaneous wetted surface of the buoy,  $S$  [27]

$$F_{fk} = - \int \int \vec{P}(t) \cdot \hat{n} dS \quad (3)$$

where  $\hat{n}$  is the unit vector pointing outwards from the buoy's surface. The pressure will be approximated using Airy's Wave Theory shown in Equation (4)

$$P(t) = \rho g e^{\chi z} A \cos(\omega t) - \rho g z \quad (4)$$

where  $\rho$  is the density of water,  $g$  is the gravity acceleration constant, and  $\chi$  is the wave number. The two terms of  $\vec{P}(t)$ , after substitution into Equation (3), give the dynamic and static FK forces used in Equation (1).

$$F_{fk} = F_{fk,d} + F_{fk,s} \quad (5)$$

The approach of Giorgi and Ringwood [27] is used to obtain closed-form expressions for the FK forces shown in Equation (6) where cylindrical coordinates are used when integrating Equation (3).

$$\begin{aligned} F_{fk,s} &= -\rho g \int_0^{2\pi} \int_{z_1}^{z_2} z f(z) f'(z) dz d\theta \\ F_{fk,d} &= -\rho g A \cos(\omega t) \int_0^{2\pi} \int_{z_1}^{z_2} e^{\chi z} f(z) f'(z) dz d\theta \end{aligned} \quad (6)$$

The revolution profile for the hourglass buoy geometry of Figure 1 is  $f(z) = \bar{\alpha}(z + h)$  for the lower cone and  $f(z) = \bar{\alpha}(z - \zeta + \eta)$  for the upper cone with  $\bar{\alpha} = \tan(\alpha)$ . The cylindrical coordinate rotation limits,  $[0, 2\pi]$ , and the vertical limits,  $[z_1, z_2]$ , are based on the instantaneous wetted surface with again with two parts: (1) the immersed portion of the lower cone with vertical limits  $[-h, 0]$  and the immersed part of the upper cone with limits  $[\zeta - \eta, 0]$ . The resulting FK force terms are given in Equation (7) where the first term of  $F_{fk,s}$  is the weight of the buoy,  $F_g$ .

$$\begin{aligned} F_{fk,s} &= \frac{1}{3} \pi \rho g \bar{\alpha}^2 [h^3 + (\eta - \zeta)^3] \\ F_{fk,d} &= \frac{2\pi}{\chi^2} \rho g \bar{\alpha}^2 \eta [2 - e^{-\chi h} - e^{-\chi(\eta - \zeta)} - \chi(h + \eta - \zeta)] \end{aligned} \quad (7)$$

Rewriting Equation (7) for substitution into Equation (1) yields Equation (8) where the first equation is the buoyancy force and is the same as developed in [17] using a geometric approach.

$$\begin{aligned} F_b = F_{fk,s} + F_g &= \frac{1}{3}\pi\rho g\bar{\alpha}^2(\eta - \zeta)^3 \\ F_{fk,d} &= \frac{2\pi}{\chi^2}\rho g\bar{\alpha}^2\eta \left[ 2 - e^{-\chi h} - e^{-\chi(\eta - \zeta)} - \chi(h + \eta - \zeta) \right] \end{aligned} \quad (8)$$

## 2.2. Radiation Force

Although not entirely consistent with the large motion assumption mentioned earlier, a linear radiation force model is used here to keep the focus on the effect of the FK forces. The radiation forces are split into two components, one related to velocity and the other to acceleration, shown in Equation (9) [30],

$$F_r = \int_0^\infty h_r(\tau)\dot{\zeta}(t - \tau)d\tau - m_a\ddot{\zeta} \quad (9)$$

where  $h_r$  is the radiation impulse response function and  $m_a$  is the added mass. However, in our analysis, we consider regular harmonic waves of Equation (2) where the integral of Equation (9) becomes Equation (10).

$$F_r = -b\dot{\zeta} - m_a\ddot{\zeta} \quad (10)$$

where  $b$  is the linear damping constant specific to the regular wave frequency. Substituting Equation (10) and Equation (8) into Equation (1), and neglecting the diffraction force yields the nonlinear model we will use for the rest of the analysis.

$$M\ddot{\zeta} + b\dot{\zeta} - \frac{1}{3}\pi\rho g\bar{\alpha}^2(\eta - \zeta)^3 - \frac{2\pi}{\chi^2}\rho g\bar{\alpha}^2\eta \left[ 2 - e^{-\chi h} - e^{-\chi(\eta - \zeta)} - \chi(h + \eta - \zeta) \right] = F_c \quad (11)$$

where  $M = m + m_a$ .

A point absorber is often modeled using the Cummins equation shown in Equation (12) [8,38,39].

$$M\ddot{\zeta} + \int_0^\infty h_r(\tau)\dot{\zeta}(t - \tau)d\tau + k\zeta = f_f \quad (12)$$

where  $f_f$  contains all external forces applied to the buoy, including diffraction, and those supplied by the power take-off. It is instructive to compare Equation (12) to the nonlinear model of Equation (11). The first two terms were introduced in Section 2.2. The third term of Equation (12),  $k\zeta$ , models the linear hydrostatic force and is valid for small motions about an equilibrium. This is replaced with a cubic term in Equation (11) appropriate for potentially large vertical displacement. The fourth term on the right of Equation (11) is the dynamic Froude–Krylov force and could be included in the  $f_f$  of Equation (12) as it can be classified as an external force. Typically, the  $f_f$  includes the linear diffraction force, which we have neglected as mentioned previously, and the PTO control force,  $F_c$  of Equation (11).

## 3. Contribution of Froude–Krylov Forces to the Free Response

Before exploring the control system design of Section 4, it is helpful to examine the relative effects of the terms in Equation (11). Instead of a nondimensional assessment, we will use the example buoy used for the control system design and rewrite Equation (11) as

$$M\ddot{\zeta} + b\dot{\zeta} - F_b - F_{fk,d} = F_c \quad (13)$$

The buoy characteristics are given in Table 1, where  $m_a$  and  $b$  were obtained using WAMIT for the buoy geometry of Figure 1. The incident regular, linear wave has a period



of 18 s and an amplitude of  $A = 0.35$  m. The amplitude was selected to yield maximum buoy displacement such that it nearly leaves the water. While this is not physically possible for a free-floating buoy, it provides a limiting scenario. Assuming the water depth,  $h_w$ , is large such that  $\chi h_w \gg 1$ , the dispersion equation.

$$\omega^2 = g\chi \tanh(\chi h_w) \approx g\chi \quad (14)$$

gives  $\chi \approx \frac{\omega^2}{g} = 0.0125$  with wavelength  $\lambda = \frac{2\pi}{\chi} = 502.65$  m.

**Table 1.** Hourglass buoy parameters.

Feature	Symbol	Value	Units
Height	$2h$	5	m
Cone Angle	$\alpha$	60	degree
Draft	$h_0$	2.5	m
Mass	$m$	50,376	kg
Density	$\rho_b$	1000	kg/m <sup>3</sup>
Added Mass	$m_a$	59,250	kg
Damping	$b$	20,000	N/(m/s)

It should be noted that under some conditions, the dynamic FK force is small compared to  $F_b$  and could be neglected. For example, for large wavelength, small wave amplitudes, small buoy displacements, and small buoy size such that  $\chi\eta \ll 1$ ,  $\chi\zeta \ll 1$  and,  $\chi h \ll 1$ , the Taylor series expansion of Equation (8) gives  $F_{fk,d} \approx 0$ .

A Simulink simulation using a fixed-step solver, ODE3, with a 0.01 s time step was created using Equation (13) where the dynamic FK force could be selectively included. The model parameters are provided in Table 1 where the hydrodynamic coefficients  $m_a$  and  $b$  were calculated using WAMIT's boundary-element-method solver [40]. The hourglass buoy geometry was discretized by a 221-panel mesh, and the solution was calculated over the angular frequency range of 0.1–12 rad/s with 0.01 rad/s increments. The equilibrium configuration was with the buoy submerged to its halfway point. To check convergence, the mesh was increased to 349 panels yielding nearly identical results as the 221-panel model. Figure 2 compares the three noninertial forces of Equation (11), as well as their sum, for the regular wave described above with  $F_c = 0$ . The buoyancy and dynamic FK forces,  $F_b$  and  $F_{fk,d}$ , are of similar amplitude but phase shifted nearly 180°. The radiation damping force,  $b\dot{\zeta}$ , is small in comparison. The force sum is also shown and illustrates an interesting result arising from the combination of  $F_b$  and  $F_{fk,d}$ . Namely, the force sum changes sign often, which is not the case if  $F_{fk,d}$  is omitted. This has a dramatic effect on the buoy motion.

To further investigate the effect of the combination of  $F_b$  and  $F_{fk,d}$  a simulation was performed with  $F_{fk,d} = 0$  with the results shown in Figure 3. For these conditions, the buoy behaves as a wave-follower with very little vertical motion and thus very low  $F_b$ , about 15 kN compared to the 600 kN of Figure 2. When  $F_{fk,d}$  is omitted, the buoy response cannot fully excite its buoyancy force's nonlinearity. In contrast, when  $F_{fk,d}$  is included, the buoy motion is excited, effectively turning on the nonlinearity that leads to even greater motion.

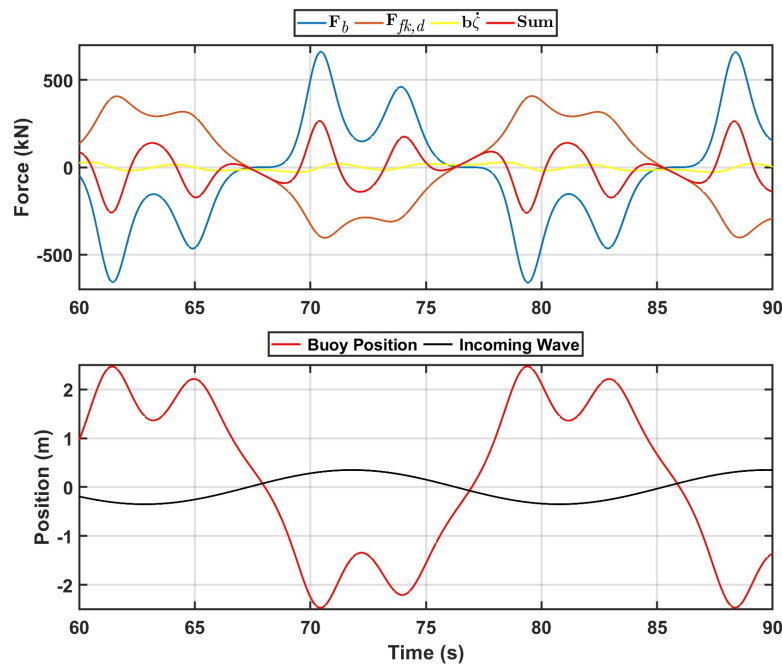


**Figure 2.** Simulated steady state results comparing the three noninertial terms of Equation (11):  $F_b = F_{fk,s} + F_g$ ,  $F_{fk,d}$ ,  $b\dot{\zeta}$  and their sum (upper plot) and the buoy displacement and wave elevation (lower plot) for a deep water wave with  $T = 18$  s and the buoy parameters shown in Table 1.

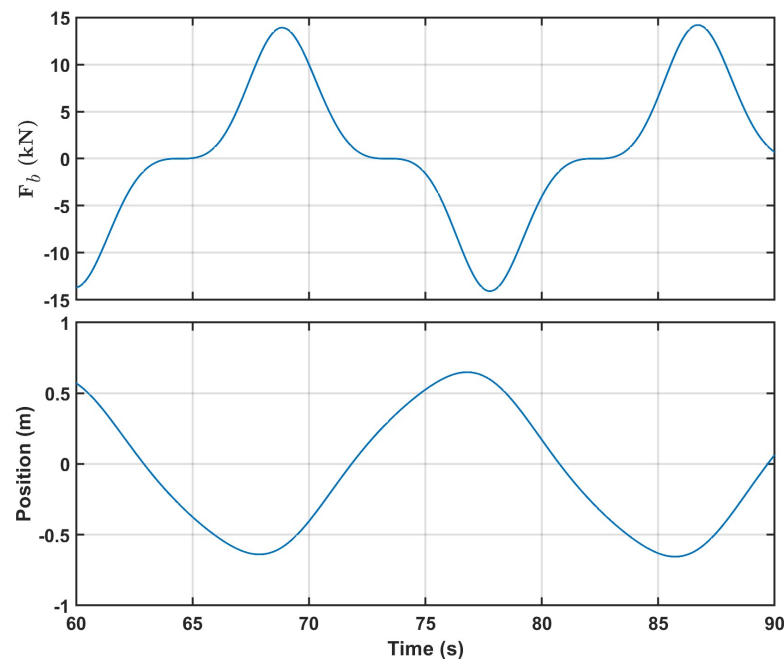


**Figure 3.** Simulated steady state results of a model without  $F_{fk,d}$ . The upper plot is  $F_b = F_{fk,s} + F_g$  force and the lower plot is the buoy displacement.

#### 4. Control Design

A general control architecture for extracting energy is shown in Figure 4, where it is assumed the instantaneous displacement states, wave elevation  $\eta$ , and the reference displacement states,  $\zeta_r$ ,  $\dot{\zeta}_r$  and  $\ddot{\zeta}_r$  are known. A variety of control laws could be used with this architecture, where we will consider feedback linearization with a sinusoidal reference to illustrate a model-based approach. It should be noted that this results in the cancellation of all the nonlinear terms in Equation (13). Such cancellation is avoided by



including these terms in the reference command leading to a control solution that does not require a reference and relies on exploiting the buoy's nonlinear response to extract energy.

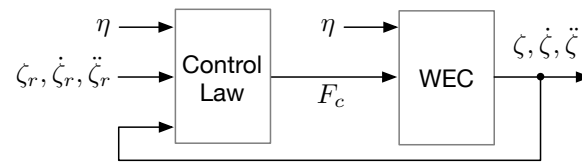


**Figure 4.** Control architecture illustrating its access to wave elevation, buoy states, and reference states.

The error states are defined by Equation (15)

$$\begin{aligned} e_1 &= \zeta - \zeta_r \\ e_2 &= \dot{\zeta} - \dot{\zeta}_r \end{aligned} \quad (15)$$

and then differentiated to form Equation (16).

$$\begin{aligned} \dot{e}_1 &= e_2 \\ \dot{e}_2 &= \ddot{\zeta} - \ddot{\zeta}_r \end{aligned} \quad (16)$$

Equation (11) can be solved for  $\ddot{\zeta}$

$$\begin{aligned} \ddot{\zeta} = M^{-1} & \left( F_c - b\dot{\zeta} + \frac{1}{3}\pi\rho g\bar{\alpha}^2(\eta - \zeta)^3 \right. \\ & \left. + \frac{2\pi}{\chi^2}\rho g\bar{\alpha}^2\eta \left[ 2 - e^{-\chi h} - e^{-\chi(\eta - \zeta)} - \chi(h + \eta - \zeta) \right] \right) \end{aligned} \quad (17)$$

and substituted into  $\dot{e}_2$  of Equation (16) to create Equation (18)

$$\dot{e}_2 = \nu - \frac{b}{M}e_2 \quad (18)$$

where  $\nu$  is:

$$\begin{aligned} \nu = M^{-1} & \left( F_c - b\dot{\zeta}_r + \frac{1}{3}\pi\rho g\bar{\alpha}^2(\eta - \zeta)^3 \right. \\ & \left. + \frac{2\pi}{\chi^2}\rho g\bar{\alpha}^2\eta \left[ 2 - e^{-\chi h} - e^{-\chi(\eta - \zeta)} - \chi(h + \eta - \zeta) \right] \right) - \ddot{\zeta}_r \end{aligned} \quad (19)$$

and the error state system of Equation (16) is written compactly in Equation (20).

$$\begin{aligned} \dot{e}_1 &= e_2 \\ \dot{e}_2 &= -\frac{b}{M}e_2 + \nu \end{aligned} \quad (20)$$

State feedback control

$$\nu = -\vec{k}^T \vec{e} \quad (21)$$

is applied to  $\nu$  and the control law is Equation (22)

$$\begin{aligned} F_c = -M\vec{k}^T \vec{e} + M\ddot{\zeta}_r + b\dot{\zeta}_r - \frac{1}{3}\pi\rho g\bar{\alpha}^2(\eta - \zeta)^3 \\ - \frac{2\pi}{\chi^2}\rho g\bar{\alpha}^2\eta \left[ 2 - e^{-\chi h} - e^{-\chi(\eta - \zeta)} - \chi(h + \eta - \zeta) \right] \end{aligned} \quad (22)$$

which is simply Equation (23).

$$F_c = -M\vec{k}^T \vec{e} + M\ddot{\zeta}_r + b\dot{\zeta}_r - F_b - F_{fk,d} \quad (23)$$

A variety of methods can be used to create the gain vector  $\vec{k}$ , where the infinite horizon, linear quadratic regulator approach is used, which minimizes the cost function of Equation (24) [41]

$$J = \int_0^{\infty} (\vec{e}^T Q \vec{e} + v^T R v) dt \quad (24)$$

where in our case

$$Q = \begin{bmatrix} 10 & 0 \\ 0 & 1 \end{bmatrix} \quad \text{and} \quad R = 1 \quad (25)$$

yielding  $\vec{k}^T = [3.16 \quad 2.53]$ . The effect of varying the  $Q_{11}$  gain value, nominally set to 10, will be examined in Section 6.3.

The control law shown in the block diagram of Figure 4 can be summarized by Equation (23), the error vector of Equation (15), the hourglass buoy parameters of Table 1, the Froude–Krylov terms of Equation (8) and the gains of  $\vec{k}$  above. It requires the reference trajectory and measurements of the wave elevation and the buoy displacement states.

### 5. Spherical Buoy Model

In Section 6, the energy extraction results of applying the control law of Section 4 to the hourglass buoy and the spherical buoy of [30] are discussed. A brief description of the spherical buoy model is provided here.

The spherical buoy model form is identical to that of the hourglass buoy of Equation (13) but with different expressions for the buoyancy and dynamic FK forces shown in Equation (26)).

$$\begin{aligned} F_b &= \frac{1}{3} \pi \rho g (\eta - \zeta) [3R^2 - (\eta - \zeta)^2] \\ F_{fk,d} &= \frac{2\pi}{\chi^2} \rho g \eta \left[ 1 - e^{-\chi(\eta+R-\zeta)} - \chi \left( \eta - \zeta + R e^{-\chi(\eta+R-\zeta)} \right) \right] \end{aligned} \quad (26)$$

The control law form is the same as given in Equation (23) with  $F_b$  and  $F_{fk,d}$  of Equation (26) and the spherical buoy parameters provided above. The LQR gains are the same as those used for the hourglass buoy.

### 6. Results

The hourglass and spherical buoys described above were modeled in Simulink and simulated using a fixed-step solver, ODE3, with a 0.01 s time step. The Simulink model is shown in Figure 5 where a MATLAB Function was used to implement the buoy dynamic model. The control law was organized into a subsystem. The incident regular wave elevation of Equation (2) was  $A = 0.5$  m with a period of six seconds,  $\omega = \frac{\pi}{3}$  matching the conditions of [30]. The reference displacement,  $\zeta_r$  of Equation (27), used by the tracking control law, had the same period but with an amplitude of two meters shown in Equation (27).

$$\zeta_r = 2 \sin \left( \frac{\pi}{3} t \right) \quad (27)$$

The absorbed energy,  $E$ , was calculated using Equation (28).

$$E = \int_0^t F_c \dot{\zeta} dt \quad (28)$$

Two closed-loop cases are explored below: (1) the effect of including the nonlinear FK force in the control law and (2) a comparison between the hourglass and spherical buoys.

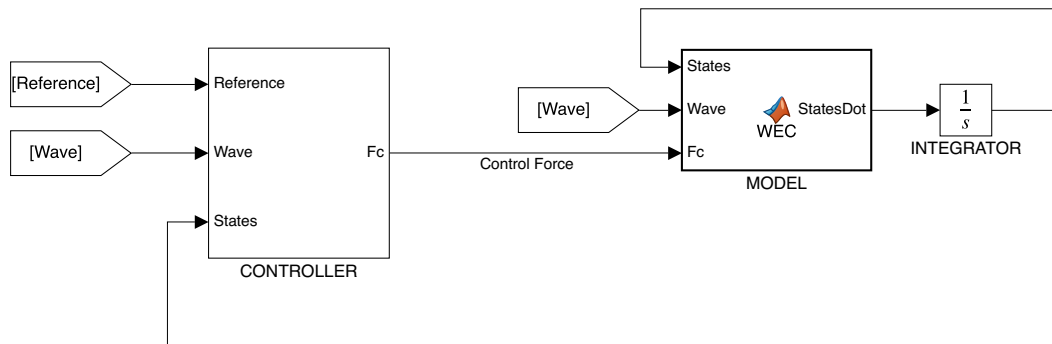


**Figure 5.** Simulink model of the closed loop system. The plant model for both the hourglass and spherical buoys was implemented using a MATLAB Function block and an integrator.

### 6.1. Effect of the Nonlinear FK Force

Calculating  $F_{fk,d}$  in the control law requires knowledge of the wave number and hence more information about the incident waves. If  $F_{fk,d}$  has negligible performance on the closed-loop energy extraction, then a model-based control strategy would be easier to implement.

Figure 6 compares the energy extraction performance of the hourglass buoy using the control law of Equation (23) with and without  $F_{fk,d}$ . The power is about 30% larger for the case where  $F_{fk,d}$  is used in the control law. As expected, the closed-loop tracking performance suffered due to the model uncertainty, as illustrated in the last two plots of Figure 6. The last plot shows the error between the reference trajectory and the buoy displacement response using  $e_1$  of Equation (15). For the case where the dynamic Froude–Krylov force is included in the control law, the error is nearly zero. In contrast, the error is about 0.8 m when the dynamic term is neglected by the control law. This same behavior is illustrated in the velocity response in the third plot. The PTO force increased slightly as the control law compensated for the model uncertainty through its error correction term. The position tracking error, shown in the last subplot, could be improved by increasing the  $\vec{k}$  of Equation (21) but was not performed here.

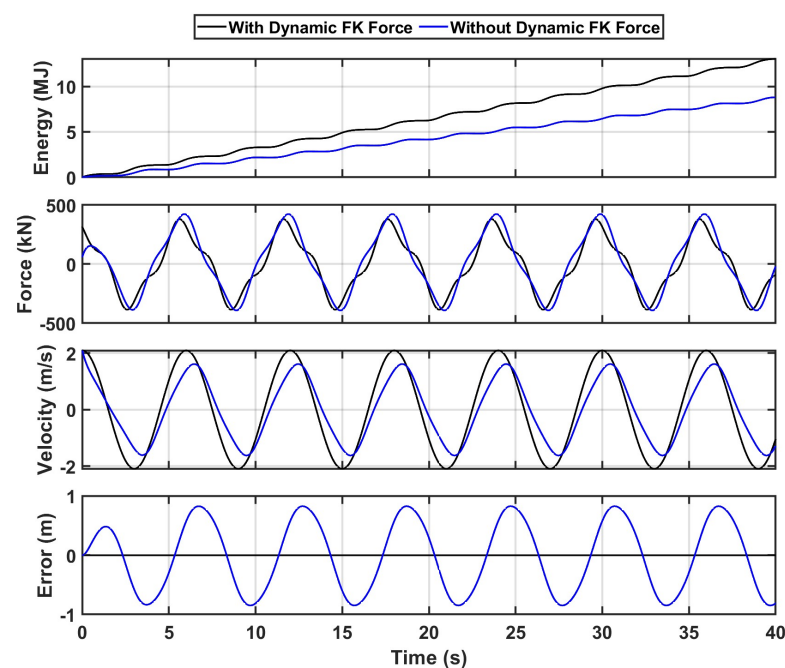


**Figure 6.** Closed-loop hourglass buoy response comparing the effect of including  $F_{fk,d}$  in the control law.

### 6.2. Hourglass and Spherical Buoy Comparison

The free-response results of Section 3 indicated that the hourglass buoy possessed synergistic behavior between its buoyancy and dynamic FK forces. In this section, we compare the closed-loop response of the hourglass buoy to a spherical one using the control law of Equation (23).

Two cases are considered: (1) a diameter of 5 m compared to the hourglass buoy whose total height was also  $2h = 5$  m, and (2) a diameter of 7.5 m so that the power generated for both buoys was approximately equal. The properties of the two spherical buoys are given in Table 2 where the added mass and damping were estimated from [42].

**Table 2.** Spherical buoy parameters.

Feature	Symbol	Case 1	Case 2	Units
Radius	$R$	2.5	3.75	m
Draft	$h_d$	2.5	3.75	m
Mass	$m$	32,725	110,446	kg
Density	$\rho_b$	500	500	kg/m <sup>3</sup>
Added Mass	$m_a$	14,019	47,492	kg
Damping	$b$	11,208	18,665	N/(m/s)

Figure 7 shows the energy extracted, control force, velocity, and position error,  $\zeta_r - \zeta$ . The energy and control force plots show the results of both buoys. Since the tracking response was nearly identical for both buoys, the velocity and position error plots are shown for only the hourglass buoy.

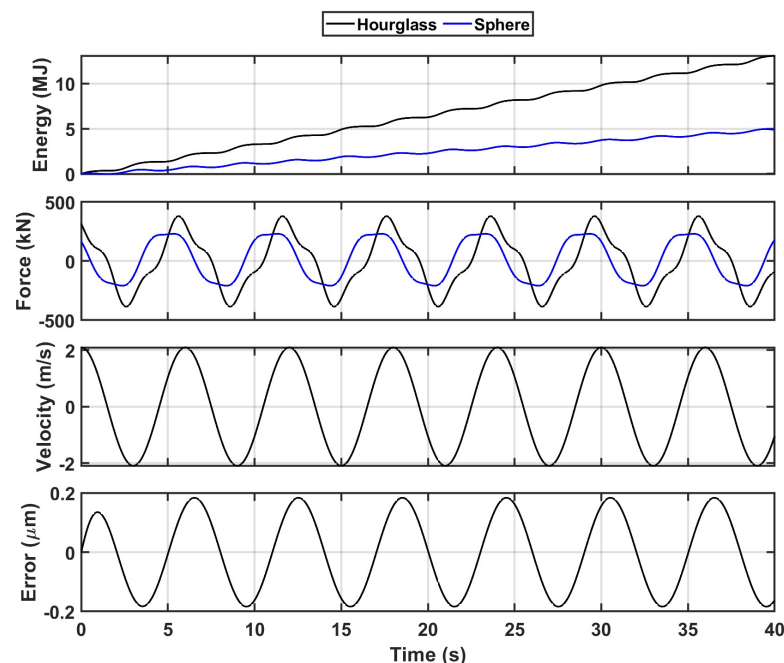


**Figure 7.** Closed-loop response and performance comparing the hourglass and spherical buoys. The hourglass buoy height and the spherical buoy diameter are both 5 m.

While the hourglass-shaped buoy shows about 160% increased energy extraction over the sphere, it should not be concluded that the hourglass shape is better than the spherical one for all conditions. An examination of the control force and velocity plots shows that the hourglass force is better aligned with the buoy velocity peaks. Thus, more energy is extracted. This could be due to differences in the mass properties of the two buoys and the effect this has on their responses resulting from their different nonlinear Froude–Krylov

force expressions. Furthermore, the hourglass buoy control amplitude is near twice that of the sphere.

To explore this further, the radius of the spherical buoy was increased to 3.75 m to yield similar energy extraction as the hourglass shown in Figure 8. This resulted in larger control forces, but the phasing between the control force and velocity was not as efficient as with the hourglass buoy for these conditions.

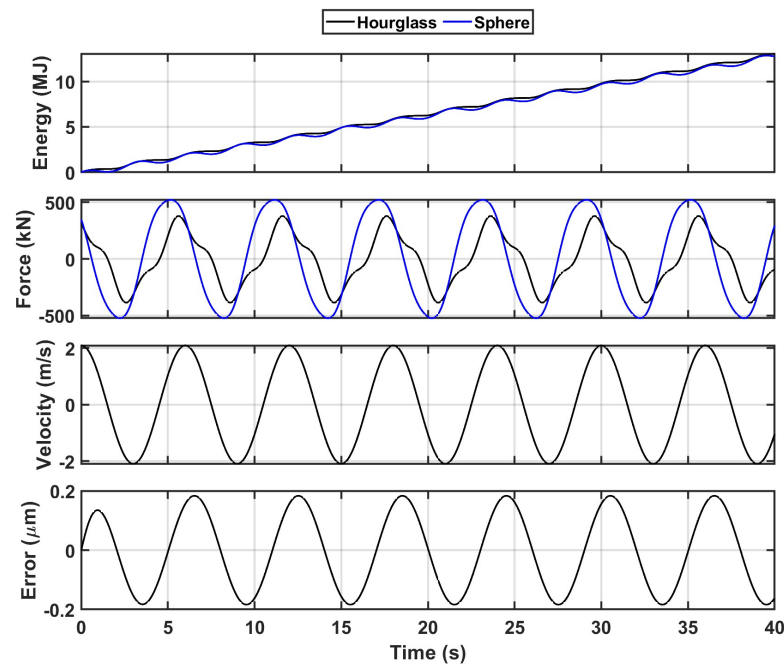


**Figure 8.** Closed-loop response and performance comparing the hourglass and spherical buoys. The hourglass buoy’s height is 5 m, and the spherical buoy diameter is 7.5 m so as to yield a similar energy extraction performance as the hourglass buoy.

A comparison of the power used in the Figures above gives a partial indicator of the WEC’s performance. As a performance metric, extracted power ignores the requirements placed on the PTO in terms of force and stroke. Equation (29) was used to capture this and allow comparison across different geometries. This power, force, amplitude (PFA) metric reduces commensurately with the PTO size in terms of maximum force and stroke.

$$PFA = \frac{A_P}{A_F A} \quad (29)$$

where  $A_P$  is the amplitude of the real power,  $A_F$  is the amplitude of the control force and  $A$  is the amplitude of the buoy position.

The PFA for the hourglass is 0.99 compared to 0.88 for the 3.75-m diameter sphere, about a 13% improvement for the hourglass buoy. Since, in both cases, the tracking control was nearly perfect, the buoy position had no effect.

### 6.3. Sensitivity Analysis

To observe the robustness of the controller, a sensitivity analysis was performed for the hourglass-shaped buoy by simultaneously increasing the added mass,  $m_a$ , and the wave number,  $\chi$ , used by the controller by 50%. The model used  $m_a = 59,250$  kg and  $\chi = 0.0125$  as described in Section 3. When these values are used by the controller, the resulting response is referred to as “Exact” whereas the “Perturbed” values were increased to  $m_a = 88,875$  kg and  $\chi = 0.0188$ .

Figure 9 shows the results where the LQR gain vector is unchanged from Section 4. The last plot shows that the tracking performance contains some errors for the perturbed

case. However, this error is sufficiently small that it did not affect the energy production or the actuator force. Table 3 shows that the displacement tracking error is reduced as the  $Q_{11}$  gain of the LQR controller is increased.

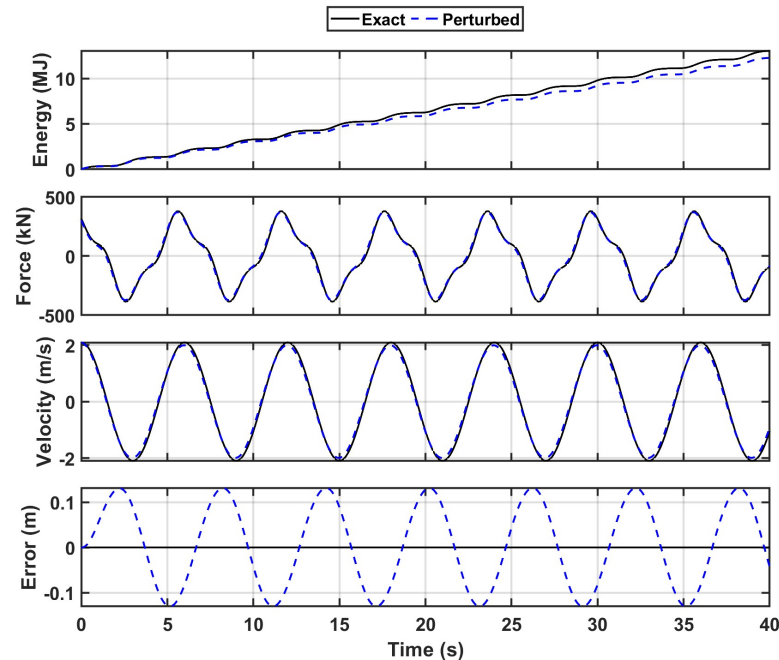


**Figure 9.** Comparison of the controller performance when using the exact model parameters and perturbed values.

**Table 3.** Displacement tracking error due to  $Q_{11}$  LQR gain value.

First State Gain	Displacement Error (m)
10	0.130
20	0.098
50	0.064
100	0.015

## 7. Conclusions and Future Work

Buoy geometry can significantly impact a point absorber's dynamic response due to the static and dynamic Froude–Krylov forces. The hourglass-shaped buoy's static and dynamic force expressions have nonlinearities of the form  $(\eta - \zeta)^3$  and  $-\eta \left[ e^{-\chi(\eta - \zeta)} + \chi(\eta - \zeta) \right]$ , respectively, as seen in Equation (8). Although the nonlinear dynamic forces are less than the static, their shape results in a total force that excites the buoy's vertical motion more than the static force alone. This additional motion results in the nonlinear terms, both static and dynamic, having an even more significant effect. Exploiting buoy shapes to create synergy between the static and dynamic forces can be used to increase the efficiency of a point absorber. While this effect is evident in the hourglass buoy, it may be possible to find shapes that are easier to implement physically, with similar synergy between their static and dynamic forces.

Model-based control usually requires reduced-order models that can execute in real time. The nonlinear dynamic forces, though less than the static, were found to impact the energy extraction of the closed-loop system. This effect will vary under different wave conditions, but they should be included when possible.

Experimental validation of static and dynamic Froude–Krylov force expressions for the hourglass buoy is one of the next steps. Incorporating the effects of significant motion on added mass and radiation damping into the control law should be explored. Shape

adaptation, and its effect on the Froude–Krylov forces, is yet another feature that could be exploited to increase point absorber efficiency.

**Author Contributions:** Conceptualization, H.Y., G.P. and D.W.; Methodology, H.Y.; Validation, G.P.; Formal analysis, H.Y. and T.D.G.; Writing—original draft, H.Y.; Writing—review & editing, T.D.G., G.P. and D.W. All authors have read and agreed to the published version of the manuscript.

**Funding:** This research received no external funding.

**Data Availability Statement:** The data presented in this study are available on request from the corresponding author.

**Acknowledgments:** Sandia National Laboratories is a multimission laboratory managed and operated by National Technology & Engineering Solutions of Sandia, LLC, a wholly owned subsidiary of Honeywell International Inc., for the U.S. Department of Energy’s National Nuclear Security Administration under contract DE-NA0003525. This paper describes objective technical results and analysis. Any subjective views or opinions that might be expressed in the paper do not necessarily represent the views of the U.S. Department of Energy or the United States Government.

**Conflicts of Interest:** The authors declare no conflict of interest.

## References

1. Falnes, J. A review of wave-energy extraction. *Mar. Struct.* **2007**, *20*, 185–201. [\[CrossRef\]](#)
2. Rémoit, F.; Chatzigiannakou, M.A.; Bender, A.; Temiz, I.; Sundberg, J.; Engström, J. Deployment and maintenance of wave energy converters at the Lysekil research site: A comparative study on the use of divers and remotely-operated vehicles. *J. Mar. Sci. Eng.* **2018**, *6*, 39. [\[CrossRef\]](#)
3. Henry, A.; Doherty, K.; Cameron, L.; Whittaker, T.; Doherty, R. *Advances in the Design of the Oyster Wave Energy Converter*; RINA Marine and Offshore Renewable Energy: London, UK, 2010.
4. Lehmann, M.; Karimpour, F.; Goudey, C.A.; Jacobson, P.T.; Alam, M.R. Ocean wave energy in the United States: Current status and future perspectives. *Renew. Sustain. Energy Rev.* **2017**, *74*, 1300–1313. [\[CrossRef\]](#)
5. Drew, B.; Plummer, A.R.; Sahinkaya, M.N. A review of wave energy converter technology. *Proc. Inst. Mech. Eng. Part A J. Power Energy* **2009**, *223*, 887–902. [\[CrossRef\]](#)
6. Budar, K.; Falnes, J. A resonant point absorber of ocean-wave power. *Nature* **1975**, *256*, 478–479. [\[CrossRef\]](#)
7. Falnes, J.; Kurniawan, A. *Ocean Waves and Oscillating Systems: Linear Interactions Including Wave-Energy Extraction*; Cambridge University Press: Cambridge, UK, 2020; Volume 8.
8. Korde, U.A.; Ringwood, J. *Hydrodynamic Control of Wave Energy Devices*; Cambridge University Press: Cambridge, UK, 2016.
9. Faedo, N.; Pasta, E.; Carapellese, F.; Orlando, V.; Pizzirusso, D.; Basile, D.; Sirigu, S.A. Energy-maximising experimental control synthesis via impedance-matching for a multi degree-of-freedom wave energy converter. *IFAC-PapersOnLine* **2022**, *55*, 345–350. [\[CrossRef\]](#)
10. Lattanzio, S.; Scruggs, J. Maximum power generation of a wave energy converter in a stochastic environment. In Proceedings of the 2011 IEEE International Conference on Control Applications (CCA), Denver, CO, USA, 28–30 September 2011; pp. 1125–1130.
11. Bacelli, G.; Nevarez, V.; Coe, R.G.; Wilson, D.G. Feedback resonating control for a wave energy converter. *IEEE Trans. Ind. Appl.* **2019**, *56*, 1862–1868. [\[CrossRef\]](#)
12. Zou, S.; Abdelkhalik, O.; Robinett, R.; Bacelli, G.; Wilson, D. Optimal control of wave energy converters. *Renew. Energy* **2017**, *103*, 217–225. [\[CrossRef\]](#)
13. Abdelkhalik, O.; Darani, S. Optimization of nonlinear wave energy converters. *Ocean. Eng.* **2018**, *162*, 187–195. [\[CrossRef\]](#)
14. Li, G.; Belmont, M.R. Model predictive control of sea wave energy converters—Part I: A convex approach for the case of a single device. *Renew. Energy* **2014**, *69*, 453–463. [\[CrossRef\]](#)
15. Brekken, T.K. On model predictive control for a point absorber wave energy converter. In Proceedings of the 2011 IEEE Trondheim PowerTech, Trondheim, Norway, 19–23 June 2011; pp. 1–8.
16. Zou, S.; Abdelkhalik, O.; Robinett, R.; Korde, U.; Bacelli, G.; Wilson, D.; Coe, R. Model Predictive Control of parametric excited pitch-surge modes in wave energy converters. *Int. J. Mar. Energy* **2017**, *19*, 32–46. [\[CrossRef\]](#)
17. Wilson, D.G.; Robinett, R.D., III; Bacelli, G.; Abdelkhalik, O.; Coe, R.G. Extending Complex Conjugate Control to Nonlinear Wave Energy Converters. *J. Mar. Sci. Eng.* **2020**, *8*, 84. [\[CrossRef\]](#)
18. Richter, M.; Magana, M.E.; Sawodny, O.; Brekken, T.K. Nonlinear model predictive control of a point absorber wave energy converter. *IEEE Trans. Sustain. Energy* **2012**, *4*, 118–126. [\[CrossRef\]](#)
19. Darani, S.; Abdelkhalik, O.; Robinett, R.D.; Wilson, D. A hamiltonian surface-shaping approach for control system analysis and the design of nonlinear wave energy converters. *J. Mar. Sci. Eng.* **2019**, *7*, 48. [\[CrossRef\]](#)
20. Wilson, D.G.; Robinett, R.D.; Bacelli, G.; Abdelkhalik, O.; Weaver, W.W.; Coe, R. Nonlinear WEC optimized geometric buoy design for efficient reactive power requirements. In Proceedings of the OCEANS 2019 MTS/IEEE, Seattle, WA, USA, 27–31 October 2019; pp. 1–6.



21. Wilson, D.G.; Robinett, R.D.; Weaver, W.W.; Glover, S.F. Wave Energy Converter Buoy with Variable Geometry that Improves Energy and Power Capture for Changing Sea States. In Proceedings of the 2022 International Symposium on Power Electronics, Electrical Drives, Automation and Motion (SPEEDAM), Sorrento, Italy, 22–24 June 2022; pp. 918–923.
22. Bacelli, G.; Coe, R.G. Comments on control of wave energy converters. *IEEE Trans. Control Syst. Technol.* **2020**, *29*, 478–481. [\[CrossRef\]](#)
23. Garcia-Rosa, P.B.; Bacelli, G.; Ringwood, J.V. Control-informed geometric optimization of wave energy converters: The impact of device motion and force constraints. *Energies* **2015**, *8*, 13672–13687. [\[CrossRef\]](#)
24. Garcia-Rosa, P.B.; Ringwood, J.V. On the sensitivity of optimal wave energy device geometry to the energy maximizing control system. *IEEE Trans. Sustain. Energy* **2015**, *7*, 419–426. [\[CrossRef\]](#)
25. Abdelkhalik, O.; Coe, R.G.; Bacelli, G.; Wilson, D.G. WEC geometry optimization with advanced control. In Proceedings of the ASME International Conference on Offshore Mechanics and Arctic Engineering, Trondheim, Norway, 25–30 June 2017; Volume 57786, p. V010T09A031.
26. Giorgi, G.; Ringwood, J.V. Implementation of latching control in a numerical wave tank with regular waves. *J. Ocean. Eng. Mar. Energy* **2016**, *2*, 211–226. [\[CrossRef\]](#)
27. Giorgi, G.; Ringwood, J.V. Computationally efficient nonlinear Froude–Krylov force calculations for heaving axisymmetric wave energy point absorbers. *J. Ocean. Eng. Mar. Energy* **2017**, *3*, 21–33. [\[CrossRef\]](#)
28. Giorgi, G.; Ringwood, J.V. A Compact 6-DoF Nonlinear Wave Energy Device Model for Power Assessment and Control Investigations. *IEEE Trans. Sustain. Energy* **2019**, *10*, 119–126. [\[CrossRef\]](#)
29. Giorgi, G.; Sirigu, S.; Bonfanti, M.; Bracco, G.; Mattiazzo, G. Fast nonlinear Froude–Krylov force calculation for prismatic floating platforms: A wave energy conversion application case. *J. Ocean. Eng. Mar. Energy* **2021**, *7*, 439–457. [\[CrossRef\]](#)
30. Demonte Gonzalez, T.; Parker, G.G.; Anderlini, E.; Weaver, W.W. Sliding mode control of a nonlinear wave energy converter model. *J. Mar. Sci. Eng.* **2021**, *9*, 951. [\[CrossRef\]](#)
31. Zou, S.; Song, J.; Abdelkhalik, O. A sliding mode control for wave energy converters in presence of unknown noise and nonlinearities. *Renew. Energy* **2023**, *202*, 432–441. [\[CrossRef\]](#)
32. Faedo, N.; Giorgi, G.; Ringwood, J.V.; Mattiazzo, G. Optimal control of wave energy systems considering nonlinear Froude–Krylov effects: Control-oriented modelling and moment-based control. *Nonlinear Dyn.* **2022**, *109*, 1777–1804. [\[CrossRef\]](#)
33. Penalba, M.; Giorgi, G.; Ringwood, J.V. Mathematical modelling of wave energy converters: A review of nonlinear approaches. *Renew. Sustain. Energy Rev.* **2017**, *78*, 1188–1207. [\[CrossRef\]](#)
34. Giorgi, G.; Ringwood, J.V. Comparing nonlinear hydrodynamic forces in heaving point absorbers and oscillating wave surge converters. *J. Ocean. Eng. Mar. Energy* **2018**, *4*, 25–35. [\[CrossRef\]](#)
35. Wilson, D.G.; Robinett, R., III; Abdelkhalik, O.; Bacelli, G. *Nonlinear Control Design for Nonlinear Wave Energy Converters*; Technical Report SAND2018-5214C; Sandia National Lab. (SNL-NM): Albuquerque, NM, USA, 2018.
36. Tan, J.; Polinder, H.; Laguna, A.J.; Miedema, S. A numerical study on the performance of the point absorber Wave Energy Converter integrated with an adjustable draft system. *Ocean. Eng.* **2022**, *254*, 111347. [\[CrossRef\]](#)
37. Forehand, D.I.; Kiprakis, A.E.; Nambiar, A.J.; Wallace, A.R. A fully coupled wave-to-wire model of an array of wave energy converters. *IEEE Trans. Sustain. Energy* **2015**, *7*, 118–128. [\[CrossRef\]](#)
38. Cummins, W. The Impulse Response Function and Ship Motions. *Schiffstechnik* **1962**, *47*, 101–109.
39. Zou, M.; Chen, M.; Zhu, L.; Li, L.; Zhao, W. A constant parameter time domain model for dynamic modelling of multi-body system with strong hydrodynamic interactions. *Ocean. Eng.* **2023**, *268*, 113376. [\[CrossRef\]](#)
40. WAMIT Inc. *The State of the Art in Wave Interaction Analysis*; WAMIT Inc.: Chestnut Hill, MA, USA, 2023.
41. Hendricks, E.; Jannerup, O.; Sørensen, P.H. *Linear Systems Control: Deterministic and Stochastic Methods*; Springer: Berlin/Heidelberg, Germany, 2008.
42. Havelock, T.H. Waves due to a floating sphere making periodic heaving oscillations. *Proc. R. Soc. Lond. Ser. A Math. Phys. Sci.* **1955**, *231*, 1–7.

**Disclaimer/Publisher’s Note:** The statements, opinions and data contained in all publications are solely those of the individual author(s) and contributor(s) and not of MDPI and/or the editor(s). MDPI and/or the editor(s) disclaim responsibility for any injury to people or property resulting from any ideas, methods, instructions or products referred to in the content.